Available online at www.sciencedirect.com
SCIENCE DIRECT®
Journal of Photochemistry and Photobiology A: Chemistry 157 (2003) 149–160
Journal of Photochemistry and Photobiology A:Chemistry
www.elsevier.com/locate/jphotochem

New measurements of OClO absorption cross-sections in the 325–435 nm region and their temperature dependence between 213 and 293 K

H. Kromminga [a,*], J. Orphal [a,b], P. Spietz [a], S. Voigt [a], J.P. Burrows [a]

[a] *Institute of Environmental Physics, University of Bremen, P.O. Box 330440, D-28334 Bremen, Germany*
[b] *Laboratoire de Photophysique Moléculaire, CNRS UPR-3361, Bât. 350, Centre d'Orsay, F-91405 Orsay Cedex, France*

Received 20 September 2001; received in revised form 25 September 2002; accepted 16 October 2002

Abstract

Absorption spectra of gas-phase OClO in the 325–435 nm region (23,000–31,000 cm^{-1}) have been measured at five atmospheric temperatures between 213 and 293 K with a spectral resolution of 1.0 cm^{-1} using Fourier-transform spectroscopy. Absolute absorption cross-sections of OClO at 293 K have been determined and were also used to scale the spectra at the lower temperatures to absolute cross-sections. The results are in good agreement with previous studies of the OClO cross-sections but provide a better coverage of atmospheric temperatures. In addition, Fourier-transform spectroscopy has the advantages of an accurate wavelength calibration and of high spectral resolution. The new cross-sections are important as reference data for remote-sensing of OClO using UV-Vis absorption spectra of the Earth's atmosphere from ground and space. The new spectra were also used to fit the OClO $\tilde{A} - \tilde{X}$ electronic band centres in order to re-determine the upper state's molecular constants. In a second set of experiments we investigated the photolysis of pure OClO leading to the formation of Cl_2 and higher chlorine oxides as further products. To provide a qualitative understanding of the photolysis mechanism a chemical reaction simulation was carried out using the FACSIMILE© software.

Keywords: OClO; Cross-section; Spectroscopy; Remote-sensing

1. Introduction

Chlorine and bromine oxides play an important role in atmospheric chemistry [1]. They are involved in the catalytic cycles leading to the annual stratospheric ozone depletion in polar springtime [2,3]. Chlorine dioxide (OClO) is an important indicator for Cl-activation [4,5]. Its major stratospheric source is the reaction BrO + ClO → OClO + Br [6], a minor source being also the reaction between ClO and NO_3 [7].

$$ClO + NO_3 \rightarrow OClO + NO_2$$

Atmospheric concentrations of OClO are determined by means of UV-Vis spectroscopy using the structured absorption of OClO in this spectral region. OClO has been detected in UV-Vis spectra of the zenith sky [8–10] and is also measured on a global scale by the global ozone monitoring experiment (GOME) onboard the ERS-2 satellite [11–13]. For the retrieval of atmospheric OClO column densities, the differential optical absorption spectroscopy (DOAS) method is employed [14,15]. For this technique accurate knowledge of the molecular absorption cross-sections and their temperature dependence is indispensable. This can only be provided by dedicated laboratory measurements [16].

Although the spectrum of the $\tilde{A}^2A_2$–$\tilde{X}^2B_1$ transition of OClO has been known for long prior to this work, only four independent studies of the UV-Vis absorption cross-sections of OClO had been published. Wahner et al. [17] employed a Xenon lamp and a grating spectrometer with a resolution of 0.25 nm in the wavelength region of 240–480 nm and a diode-array detector for measurements at three different temperatures (204, 296 and 378 K). They determined absolute cross-sections based on OClO partial pressures and by reacting OClO with NO to produce NO_2. They ascertained the OClO absorption was linear and showing Beer–Lambert's law behaviour up to an optical density of 1. The bands were found to become sharper and the underlying continuum weaker with decreasing temperatures. In contrast Frost et al. [18] measured absorption OClO absorption cross-sections at 200 ± 20 K in the wavelength region 390–454 nm at a resolution of 0.5 and 0.1 cm^{-1} using a combination of Fourier-transform spectroscopy and supersonic

* Corresponding author. Tel.: +49-421-218-3526; fax: +49-421-218-4555.
E-mail address: heike.kromminga@iup.physik.uni-bremen.de (H. Kromminga).

1010-6030/03/$ – see front matter © 2003 Elsevier Science B.V. All rights reserved.
doi:10.1016/S1010-6030(03)00071-6

jet expansion but measured only relative spectra and scaled these to the previously mentioned data from Wahner et al. [17].

An important step in analysing the $\tilde{A}^2A_2$ vibrational structure of both OClO isotopes was made by Richard and Vaida [19] using a high-resolution Fourier-transform ultraviolet spectrometer together with a supersonic molecular jet. As a result of the rotational cooling the upper state vibrational energy structure has been measured and analysed in the absence of much of the spectral congestion present in the static gas spectrum. Hence, they presented a re-analysis of the vibrational progressions and harmonic and anharmonic vibrational constants for the upper electronic state.

Furthermore, Hubinger and Nee [20] measured absolute photoabsorption cross-sections between 125 and 470 nm (80,000–21,273 cm^{-1}) at room temperature using a Minuteman 0.5 m vacuum monochromator with a dispersion of 1.67 nm mm^{-1} and a PMT detector.

More recently, Marston et al. [21] published absorption cross-sections of OClO at room temperature also in the UV and VUV using synchrotron light.

In order to validate these results, to improve the accuracy of the OClO absorption cross-sections with respect to spectral calibration and resolution, and to cover a broader range of atmospheric temperatures, OClO absorption spectra in the 325–435 nm region were measured at five different temperatures between 213 and 293 K, using a Fourier-transform spectrometer (FTS). The particular advantages of FTS for recording atmospheric remote-sensing reference spectra are (1) the high wavelength accuracy of this technique, (2) the narrow and well defined instrumental line shape of the FTS, and (3) the opportunity to record high-resolution spectra over a broad spectral range.

2. Experimental

2.1. Experimental set-up

All measurements were performed using a Bruker IFS-120 HR Fourier-transform spectrometer designed for operation in the UV-Vis spectral range with a beamsplitter made of UV-Quartz. All mirrors (except for the corner-cubes) were coated with MgF_2 and selected corner-cubes were used with a high modulation efficiency even in the UV range. The instrument at the IUP Bremen is characterised by a maximum resolution of 0.004 cm^{-1} [22]. It is capable of recording spectra from the MIR to the UV regions at a high wavenumber accuracy. The wavenumber accuracy of the instrument in the UV-Vis was validated by recording absorption spectra of I_2 in the visible, showing overall agreement with reference line positions [23] of better than 0.01 cm^{-1}. For the OClO absorption spectra of this study, a resolution of 1.0 cm^{-1} (corresponding to 10 pm at 325 nm and to 19 pm at 435 nm, respectively) was selected, approximately a factor of 10 better than GOME and SCIAMACHY and other grating spectrometers used for atmospheric remote-sensing. This higher resolution is essential in order to enable convolution of the new data of this study with the instrumental line shape of the atmospheric spectrometers.

For recording the high-resolution spectra a coolable absorption cell made of Quartz with 120 cm base-length and an inner diameter of 5 cm was used. This cell is part of the so-called “calibration apparatus for trace gas absorption spectra” (CATGAS) [24], a set-up which was developed at the IUP Bremen for measuring UV-Vis reference spectra of atmospheric molecules with the GOME and SCIAMACHY satellite instruments [25–27]. Although it is possible to use a White-type multi-reflection optics with this cell, the strong absorption of OClO facilitated the use of a simple path of 1.2 m. The total absorption path thus corresponded to the length of the CATGAS cell.

The cell has a double jacket, with an ethanol coolant flow through the inner jacket and an evacuated outer part. Additionally, the cell is encased in insolating foam (Armaflex®) to provide optimal thermal stability inside. OClO spectra at five different temperatures between 293 and 213 K were recorded. The cooling of the ethanol was achieved by a two-stage cryocooler (Haake KT-90). The temperature stability for this cooling device was determined to be about ±1 K.

A super quiet Xenon arc lamp (Osram XBO 150W/2-UV) together with a water cooled elliptic mirror coated with MgF_2 (Amko GmbH) was employed as white-light source. Using this source, the entire spectral region between 20,000 and 43,000 cm^{-1} (500–217 nm) was covered. The light was coupled out of the spectrometer after traversing the interferometer chamber, which was evacuated to about 0.05 mbar during all experiments (therefore the given wavenumbers are for vacuum conditions), to pass through the outside of the spectrometer located absorption cell and reach the detector.

For the measurements in the range of the OClO absorption a room temperature GaP semiconductor diode detector (covering the wavenumber region from 20,000 to 33,000 cm^{-1}, 500–303 nm, respectively) was used in combination with a UG5-filter (Schott) to suppress strong Xenon-peaks in the near IR.

For the high-resolution absorption spectra at different temperatures, OClO was synthesised in a flow reaction described by Derby and Hutchinson [28]:

$$2NaClO_2 + Cl_2 \rightarrow 2OClO + 2NaCl.$$

Gaseous Cl_2 (pre-mix of 5% Cl_2 in synthetic air, Messer Griesheim, stated purity 99%) was passed through a Pyrex column filled with fresh $NaClO_2$ (ACROS, stated purity 88%) mixed with glass beads. A stable flow was maintained by calibrated MKS mass flow controllers. For the experiments the flow rates were in the range between 1.90 and 2.85 ml min^{-1}. Downstream, the OClO was diluted with dry N_2 (flow rates between 400 and 470 ml min^{-1}) and flushed through the coolable absorption cell. The OClO was

trapped at liquid nitrogen temperature in order to protect the pumping system. For each spectrum at different temperatures a new column with freshly prepared $NaClO_2$ was used. The cell pressure was permanently monitored by a calibrated MKS Baratron capacitance manometer with a 100 mbar head, at values between 1.0 and 11.1 mbar.

It should be noted that in a recent experimental study of OClO by Marston et al. [21], which extended into the VUV where chlorine can be easily detected, the same synthesis method was applied and no traces of remaining Cl_2 were found.

2.2. Measurement of OClO absorption spectra at different temperatures

For all temperatures (293, 273, 253, 233, and 213 K) the high-resolution OClO absorption measurements were carried out according to the following procedure.

As determined in a series of experiments prior to recording the high-resolution spectra a conditioning period of approximately 4 h was needed to achieve a steady OClO flow ensuring an optical density between 0.45 and 0.6 for different $NaClO_2$ columns with no detectable chlorine impurities with the used FTS set-up. During this conditioning period the absorption cell was cooled down to the desired temperature.

The chosen optical density of OClO was always limited to values below 1.0 in order to avoid high-resolution saturation effects of the OClO band structure. The linearity of the Beer–Lambert's law in this range was tested before, using high-resolution OClO spectra recorded previously in our group [29], see also Fig. 1. The OClO flow was diluted with dry N_2 until the desired optical densities were achieved.

Before each high-resolution measurement the cell was evacuated and then filled with the optimum N_2 flow, the OClO flow being reduced to zero. After measuring a Xenon lamp reference spectrum under this condition at a resolution of 10 cm^{-1}, the OClO flow was added again. After 5 min a high-resolution measurement of 12 individual blocks each containing 50 scans was performed. Thereafter the OClO flow was turned off and the cell was again flushed with pure N_2 for about 10 min. Then a second Xenon lamp reference spectrum was measured.

2.3. Determination of absolute absorption cross-sections at 293 K

For the determination of absolute OClO absorption cross-sections at 293 K pure OClO samples were produced by the reaction

$$3KClO_3 + 3H_2SO_4 \rightarrow 2OClO + HClO_4 + H_2O + 3KHSO_4.$$

H_2SO_4: 99% stated purity, $KClO_3$: 99% stated purity, Merck. In order to obtain high purity OClO, fractional low temperature distillations were used until the saturated vapour pressure at equal temperatures reached a minimum and the optical densities at equal pressures reached maximum values (see Fig. 2). The synthesis and the measurements were carried out in the dark to avoid photodecomposition of the samples.

In these experiments, low resolution absorption spectra of pure OClO were recorded at different total pressures (in the 0.2–0.3 mbar range) using a short Pyrex cell of 106.7 mm total length.

Pressures of 0.2–0.3 mbar of OClO were filled into the short-path absorption cell at room temperature (293 K). The statistical uncertainty of the pressure measurement was determined to be 0.13% (using different reference volumes connected to the cell and a calibrated pressure head). After filling the cell, an OClO absorption spectrum was recorded

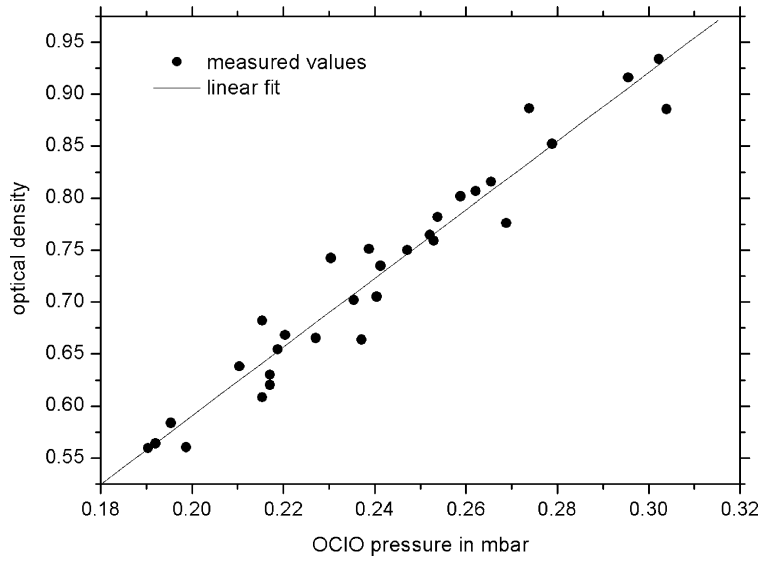

Fig. 1. Linearity of the optical density ln (I_0/I) at 351 nm (28,490 cm^{-1}) as a function of OClO pressure. The spectral resolution is 20 cm^{-1}.

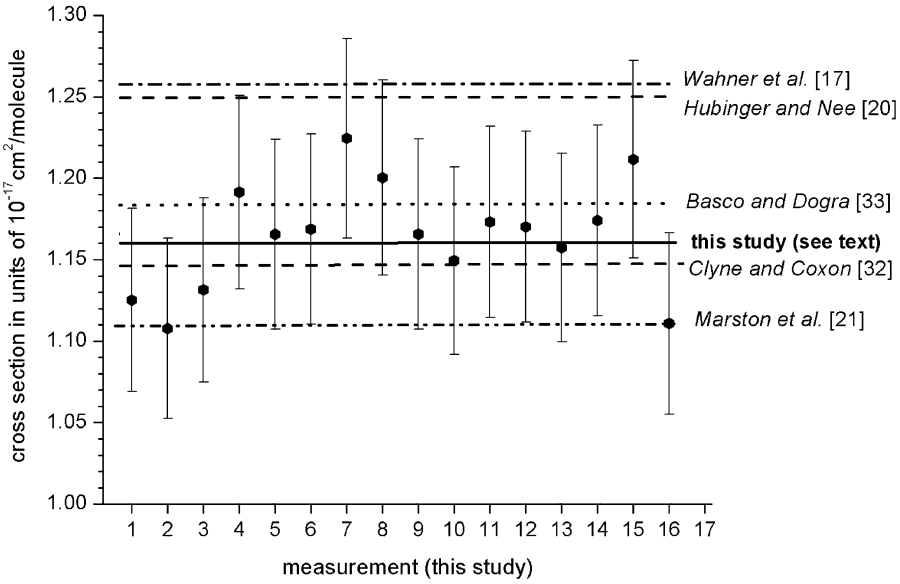

Fig. 2. The OClO absorption cross-section at 351 nm (28,490 cm^{-1}) (spectral resolution 20 cm^{-1}, temperature 300 K) for different measurements of this study. Each measurement was performed with a fresh OClO sample obtained by distillation into the absorption cell. Also shown are cross-sections from previous studies [17,20,21,33,34]. The error limits for Wahner et al. [17] are about ±10%, for Hubinger and Nee [20] about ±9% and for Marston et al. [21] about ±15%.

at a resolution of 20 cm^{-1} (corresponding to about 0.21 nm at 325 nm and to 0.38 nm at 435 nm, respectively). In order to ensure that no saturation effects occur at these optical densities, the linearity of the optical density at 351 nm was verified (see Fig. 1).

2.4. Photolysis of OClO

The photolysis experiments were carried out to validate the results from the measurements at 293 K using pure OClO. Therefore the short-path Pyrex cell was filled with an initial OClO pressure of about 2.3 mbar. Even if Cl_2 and O_2 were the only photolysis products of OClO, it would be difficult or impossible to detect the chlorine when using smaller initial amounts of OClO. The maximum absorption cross-section of Cl_2 between 300 and 400 nm is about 4.0×10^{-19} cm^2 per molecule (i.e. about 50 times weaker than the peak cross-sections of OClO at 351 nm, which is about 1.2×10^{-17} cm^2 per molecule).

The optical set-up for the photolysis experiment consisted of the same small absorption cell used for the total pressure experiments, i.e. the Xenon lamp as white-light source and the GaP semiconductor diode as detector. A Quartz–Tungsten–Halogen lamp (Osram, 50 W) installed near to the absorption cell was employed as a broad-band photolysis light source. The following measurement procedure was applied: first an OClO absorption spectrum was measured, then OClO was photolysed for about 10 min. Afterwards the absorption spectrum of the photolysis products was recorded. Finally a reference spectrum of the empty cell was measured.

3. Data reduction

For each temperature the high-resolution absorption spectra were measured in 12 blocks of 50 scans each. The lamp reference spectra were measured before and after the measurement of the absorption spectra. From both lamp spectra a weighted spectrum $I_{0,w}(\nu, T)$ was calculated for each block of high-resolution absorption spectra in order to account for lamp drifts, thus minimising the baseline errors. The resulting optical densities $OD(\nu, T)$ were calculated from the weighted lamp spectrum $I_{0,w}(\nu, T)$ and the absorption spectrum $I(\nu, T)$ as follows:

$$OD(\nu, T) = -\ln \frac{I(\nu, T)}{I_{0,w}(\nu, T)}.$$

For each temperature the optical densities of the 12 measured spectra were averaged.

For the photolysis experiments, in which the same short-path absorption cell was used, the high OClO optical density of about 7 around 28,448 cm^{-1} (ca. 351 nm) caused saturation for the strong bands. Therefore, the optical density at this wavenumber was calculated using a much weaker peak at 24,042 cm^{-1}. The ratio between the two peaks was determined previously from the 31 spectra recorded at known OClO pressures. The statistical uncertainty when deriving the maximum absorption using this method was assessed to be about 3% (rms).

The high-resolution optical density spectrum at 293 K was first convoluted to a 20 cm^{-1} resolution to match the OClO spectra recorded at known pressures and then scaled to

absolute absorption cross-section from the latter measurements. For all other temperatures (273, 253, 233, and 213 K), for each spectrum the integrated optical density between 22,700 and 31,000 cm^{-1} was calculated, normalised to unity, and then multiplied with the integrated absorption cross-section of OClO at room temperature, in order to obtain absolute absorption cross-sections at the temperatures below 293 K. This method is justified by the fact that the OClO-spectrum in this wavenumber range arises from a transition to an excited electronic state ($\tilde{A}^2A_2 - \tilde{X}^2B_1$), so that the integrated absorption cross-section is only determined by the electronic wave functions of the upper and ground state, by their energy difference and by the electronic dipole moment operator. These quantities are all independent of temperature within the Born–Oppenheimer approximation. While the OClO spectrum changes its shape with temperature, i.e. at lower temperatures the peaks become sharper and the continuum below reduces, the integrated cross-sections, however, remain constant, for the temperature range considered.

This approach has previously been used for the UV-Vis spectra of NO_2 and O_3 [30–32], and was shown to be accurate to at least 1% in the atmospheric temperature range (190–300 K) for most atmospheric molecules, provided the Born–Oppenheimer approximation holds. It is interesting to note that the integrated OClO absorption cross-sections at three different temperatures determined from the spectra of Wahner et al. [17] agree within 3% (which is less than their stated experimental uncertainty) and show no systematic variation with temperature.

4. Results

The absorption cross-sections determined for OClO were compared with those of previous studies in Fig. 2. The resulting absolute cross-section of 1.16×10^{-17} cm^2 per molecule for the peak (11,0,0) at ~28,450 cm^{-1} (351.5 nm) with a spectral resolution of 20 cm^{-1} and at a temperature of 293 K has a statistical error of <5% due to noise and baseline-effects, cell-length, volume, temperature and pressure. This value is considered a lower limit for the accuracy of the OClO absorption cross-sections, because the presence of initial Cl_2 impurities would lead to smaller OClO cross-sections when using the total pressure for determining the OClO concentration in the absorption cell. However the amount of residual Cl_2 was estimated to be <1–2% because of the constancy of the OClO from the purified sample (see Fig. 2) once all Cl_2 was distilled off. The OClO FTS absorption cross-sections at all measured temperatures are shown in Fig. 3. They clearly show an increase of the differential structure with decreasing temperatures which is important for atmospheric remote-sensing. A detailed plot of the region used for atmospheric OClO retrieval with the GOME satellite instrument (355–379 nm, 26,400–28,000 cm^{-1}) is shown in Fig. 4.

A comparison of the cross-sections of this work at 293 and 213 K with the data of Wahner et al. [17] is shown in Fig. 5. Note that there is a clear wavenumber shift between both spectra which can not be explained by data measured in air with data from vacuum measurements alone. As mentioned above, the FTS has high wavenumber accuracy, validated using I_2 absorption lines, whereas Wahner et al.

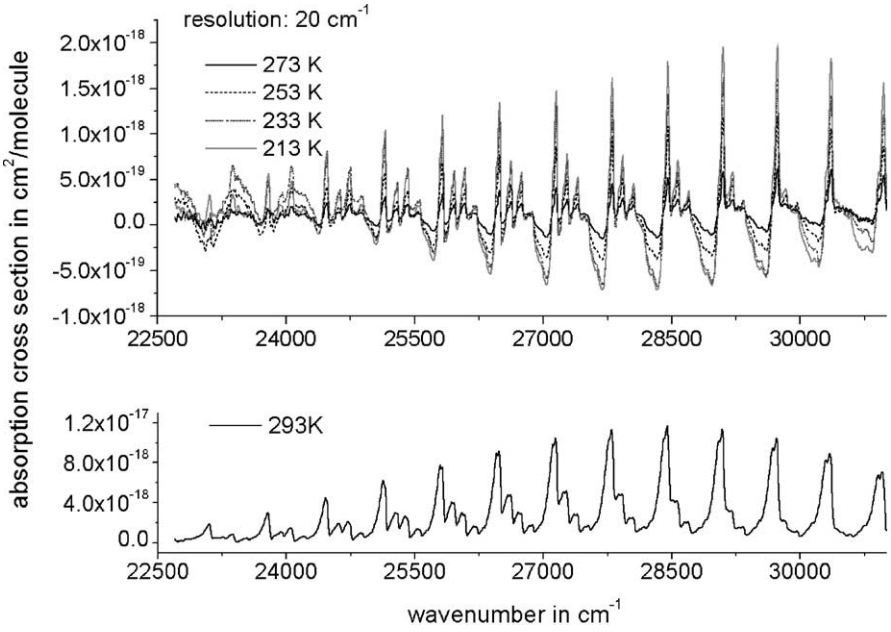

Fig. 3. The OClO cross-section of this study over the entire spectral region with a resolution of 20 cm^{-1}. The lower graph shows the room temperature spectrum. The upper graph indicates the difference between each temperature and the room temperature. Note the increase of differential structure with decreasing temperature, and the predissociation broadening of the OClO bands with increasing wavenumbers.

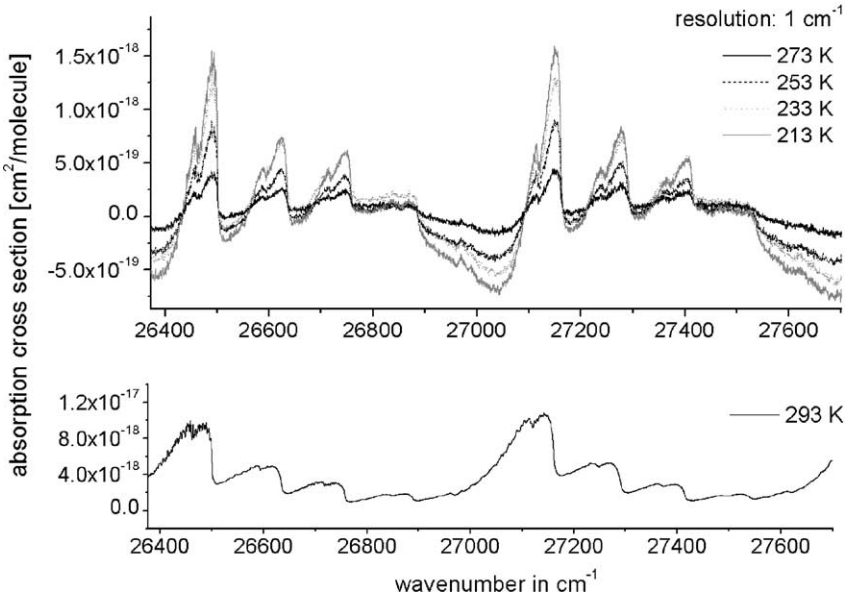

Fig. 4. The OClO cross-sections of this study at the spectral region used for atmospheric remote-sensing, resolution of 1 cm^{-1}. The lower graph shows the room temperature spectrum. The upper graph indicates the difference between each temperature and the room temperature.

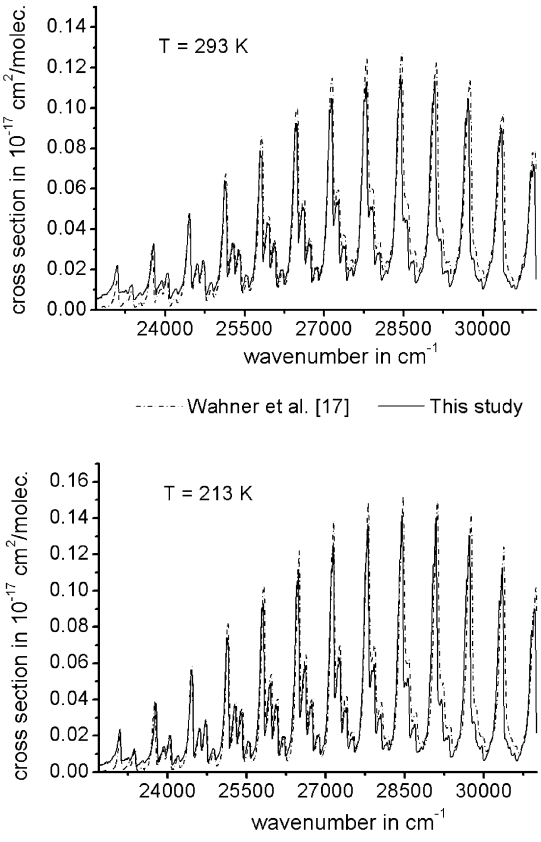

Fig. 5. Comparison of the OClO cross-sections of this study at 296 and 213 K (solid line) with the data of Wahner et al. [17] at 296 and 204 K (dotted line). There are prominent wavelength shifts probably due to wavelength calibration uncertainties in the data of Wahner et al. Note that the spectra of this study are shown at a low resolution (20 cm^{-1}) for this comparison.

[17] worked with a grating spectrometer and used only two HgCd lines for their spectral calibration. Note that an accurate wavenumber calibration is particularly important in atmospheric remote-sensing. Furthermore, the new OClO cross-sections of this study cover a wider range of temperatures and provide spectra at a higher resolution compared to previous work.

Comparison of the new FTS spectra convoluted to SCIAMACHY spectral resolution and some recent measurements using the SCIAMACHY instrument [27] shows good agreement (Fig. 6).

In Fig. 7 the vibrational assignments provided by Richard and Vaida [19] were used. Peak absorption cross-sections and bandhead positions for 293 and 213 K and at two different spectral resolutions (1 and 20 cm^{-1}) were determined and are given in Table 1. Four different band progressions for $O^{35}ClO$ could be identified for both resolutions and all temperatures though only 293 and 213 K data are given in the table.

A comparison of the new cross-sections at 293 K with the study of Hubinger and Nee [20] who worked at significantly lower spectral resolution shows quite good agreement within each error limits (±9%, overall, Fig. 2). While all absolute cross-section measurements agree within their respective uncertainties (overall variation less than ±7% compared to the mean value of about 1.18×10^{-17} cm^2 per molecule), one should note, however, that the peak cross-sections of Wahner et al. (who used two independent methods for determining their OClO amounts in the cell) and of Hubinger and Nee show excellent agreement. If these values are true the only possible explanation for the 8% difference between our peak value and those of Wahner et al. and Hubinger and Nee would be some residual Cl_2 in our absorption cell

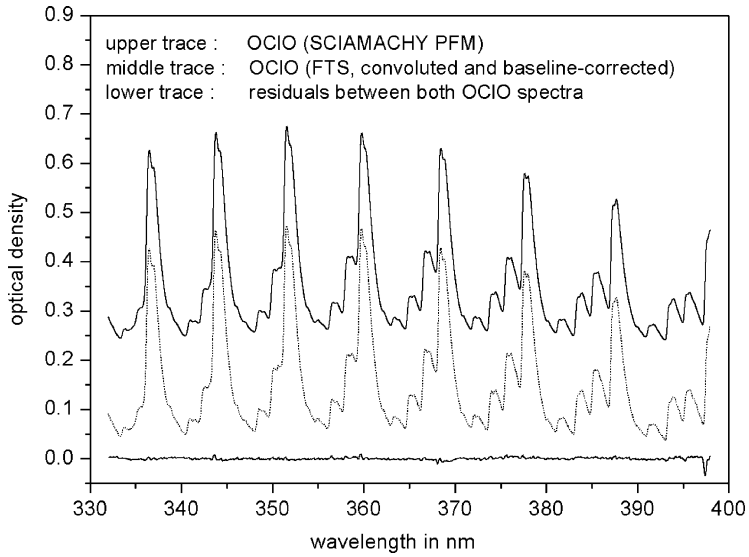

Fig. 6. Comparison of the OClO cross-sections of this study at 296 K (lower trace) with an OClO spectrum recorded with the SCIAMACHY FM [27] (upper trace, shifted for clarity). In order to account for small baseline errors and wavelength errors, and to scale the spectra to each other, a non-linear least-squares fitting routine was used [36]. Note the good agreement between both spectra. The sharp residual feature around 397 nm is due to uncorrected straylight at the edge of SCIAMACHY channel 2.

which, however, was not possible to be observed in such small amounts with our experimental set-up.

In order to be able to interpolate the OClO absorption cross-sections to intermediate temperatures, the cross-sections at each wavelength were fitted with a quadratic polynomial (temperature in °C) according to $\sigma(T) = C_1 + C_2T + C_3T^2$. In this way, the coefficients shown in Fig. 8 were determined from a least-squares fit based on the new measurements. The residuals are <4% in the entire range 26,000–30,000 cm^{-1} (340–390 nm). They are however larger in regions with small cross-sections and might therefore be at least partly due to small baseline problems in the measurement. The cross-sections derived from this simple parameter model should therefore be less influenced by baseline errors, since five different measurements (at different temperatures) were used for the determination of the polynomial coefficients. The root mean square (rms) deviation is of the same order for all temperatures and wavelengths, i.e. between 3 and 6%.

4.1. Spectral analysis

Using the spectra of this study (see the vibrational assignments in Fig. 7) we re-determined the molecular

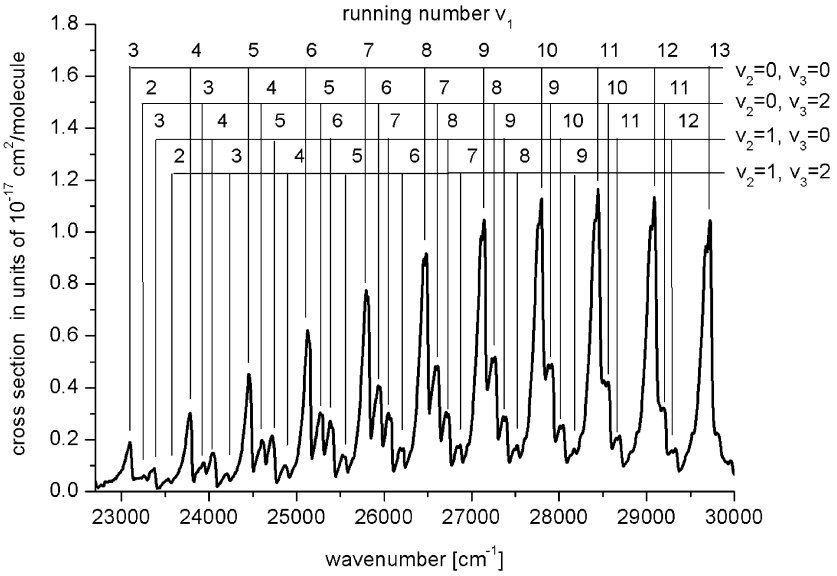

Fig. 7. The vibrational assignments of the OClO electronic bands of the $\tilde{A}^2A_2$ system recorded in this study. The assignments are taken from the analysis of Richard and Vaida [19]. Note that the bands with v_3 upper state quanta larger than 2 are very weak in these spectra.

Table 1
The observed bandheads and cross-sections of $O^{35}ClO$

	Peak position (resolution 1 cm^{-1}) (cm^{-1})	Cross-section (resolution 1 cm^{-1}) (cm^2 per molecule)	Peak position (resolution 20 cm^{-1}) (cm^{-1})	Cross-section (resolution 20 cm^{-1}) (cm^2 per molecule)
Assignment ($T = 293$ K)				
A^2A_2 system: symmetric stretch				
$\nu_{3.0.0}$	23081.6	2.76×10^{-18}	23095.4	1.90×10^{-18}
$\nu_{4.0.0}$	23783.1	4.18×10^{-18}	23783.8	3.01×10^{-18}
$\nu_{5.0.0}$	24477.3	6.00×10^{-18}	24460.7	4.50×10^{-18}
$\nu_{6.0.0}$	25139.8	7.54×10^{-18}	25143.4	5.77×10^{-18}
$\nu_{7.0.0}$	25824.6	9.03×10^{-18}	25814.5	7.50×10^{-18}
$\nu_{8.0.0}$	26489.6	9.73×10^{-18}	26479.8	9.17×10^{-18}
$\nu_{9.0.0}$	27142.3	1.08×10^{-17}	27139.4	1.05×10^{-17}
$\nu_{10.0.0}$	27798.5	1.15×10^{-17}	27798.9	1.13×10^{-17}
$\nu_{11.0.0}$	28444.7	1.19×10^{-17}	28446.9	1.16×10^{-17}
$\nu_{12.0.0}$	29085.8	1.16×10^{-17}	29089.0	1.13×10^{-17}
$\nu_{13.0.0}$	29720.0	1.06×10^{-17}	29719.6	1.04×10^{-17}
A^2A_2 system: bend				
$\nu_{2.1.0}$				
$\nu_{3.1.0}$	23372.7	1.24×10^{-18}	23373.1	8.86×10^{-19}
$\nu_{4.1.0}$	24045.3	1.95×10^{-18}	24049.9	1.49×10^{-18}
$\nu_{5.1.0}$	24744.9	2.22×10^{-18}	24721.1	2.14×10^{-18}
$\nu_{6.1.0}$	25411.3	2.71×10^{-18}	25403.7	2.47×10^{-18}
$\nu_{7.1.0}$	26077.7	3.09×10^{-18}	26074.8	2.82×10^{-18}
$\nu_{8.1.0}$	26738.7	3.10×10^{-18}	26734.4	2.98×10^{-18}
$\nu_{9.1.0}$	27390.7	2.91×10^{-18}	27393.9	2.86×10^{-18}
$\nu_{10.1.0}$	28042.6	2.62×10^{-18}	28047.7	2.55×10^{-18}
$\nu_{11.1.0}$	28685.1	2.17×10^{-18}	28689.8	2.14×10^{-18}
$\nu_{12.1.0}$	29329.5	1.73×10^{-18}	29326.2	1.65×10^{-18}
A^2A_2 system: asymmetric stretch				
$\nu_{3.0.2}$	23934.2	1.32×10^{-18}	23934.2	1.12×10^{-18}
$\nu_{4.0.2}$	24630.3	2.35×10^{-18}	24622.7	1.89×10^{-18}
$\nu_{5.0.2}$	25296.7	3.52×10^{-18}	25288.0	2.95×10^{-18}
$\nu_{6.0.2}$	25962.0	4.34×10^{-18}	25953.3	4.04×10^{-18}
$\nu_{7.0.2}$	26615.8	4.96×10^{-18}	26612.9	4.84×10^{-18}
$\nu_{8.0.2}$	27262.3	5.25×10^{-18}	27266.6	5.18×10^{-18}
$\nu_{9.0.2}$	27914.6	4.97×10^{-18}	27914.6	4.89×10^{-18}
$\nu_{10.0.2}$	28555.7	4.28×10^{-18}	28556.8	4.23×10^{-18}
$\nu_{11.0.2}$	29195.7	3.31×10^{-18}	29193.2	3.23×10^{-18}
$\nu_{12.0.2}$	29804.3	2.32×10^{-18}	29806.4	2.25×10^{-18}
A^2A_2 system: asymmetric stretch and bend				
$\nu_{2.1.2}$	23532.5	7.62×10^{-19}	23535.0	4.85×10^{-19}
$\nu_{3.1.2}$	24211.9	8.42×10^{-19}	24200.4	6.72×10^{-19}
$\nu_{4.1.2}$	24892.8	1.08×10^{-18}	24888.8	9.45×10^{-19}
$\nu_{5.1.2}$	25560.7	1.47×10^{-18}	25554.2	1.35×10^{-18}
$\nu_{6.1.2}$	26215.9	1.72×10^{-18}	26213.7	1.66×10^{-18}
$\nu_{7.1.2}$	26871.1	1.86×10^{-18}	26873.2	1.81×10^{-18}
$\nu_{8.1.2}$	27522.3	1.83×10^{-18}	27521.2	1.79×10^{-18}
$\nu_{9.1.2}$	28168.8	1.58×10^{-18}	28169.2	1.63×10^{-18}
Assignment ($T = 213$ K)				
A^2A_2 system: symmetric stretch				
$\nu_{3.0.0}$	23113.5	3.42×10^{-18}	23101.1	2.21×10^{-18}
$\nu_{4.0.0}$	23783.1	5.16×10^{-18}	23783.8	3.57×10^{-18}
$\nu_{5.0.0}$	24482.4	7.49×10^{-18}	24460.7	5.23×10^{-18}
$\nu_{6.0.0}$	25158.2	9.26×10^{-18}	25149.2	6.71×10^{-18}
$\nu_{7.0.0}$	25824.6	1.07×10^{-17}	25820.3	8.70×10^{-18}
$\nu_{8.0.0}$	26489.6	1.13×10^{-17}	26485.6	1.05×10^{-17}
$\nu_{9.0.0}$	27143.0	1.22×10^{-17}	27145.1	1.19×10^{-17}
$\nu_{10.0.0}$	27799.6	1.31×10^{-17}	27798.9	1.28×10^{-17}
$\nu_{11.0.0}$	28450.1	1.36×10^{-17}	28446.9	1.33×10^{-17}
$\nu_{12.0.0}$	29090.5	1.34×10^{-17}	29089.0	1.31×10^{-17}
$\nu_{13.0.0}$	29722.5	1.26×10^{-17}	29725.4	1.22×10^{-17}

Table 1 (*Continued*)

	Peak position (resolution 1 cm^{-1}) (cm^{-1})	Cross-section (resolution 1 cm^{-1}) (cm^2 per molecule)	Peak position (resolution 20 cm^{-1}) (cm^{-1})	Cross-section (resolution 20 cm^{-1}) (cm^2 per molecule)
A^2A_2 system: bend				
$\nu_{2.1.0}$				
$\nu_{3.1.0}$	23376.3	1.50×10^{-18}	23373.1	1.21×10^{-18}
$\nu_{4.1.0}$	24073.5	2.34×10^{-18}	24049.9	1.93×10^{-18}
$\nu_{5.1.0}$	24744.9	2.80×10^{-18}	24726.8	2.62×10^{-18}
$\nu_{6.1.0}$	25418.6	3.31×10^{-18}	25403.7	2.99×10^{-18}
$\nu_{7.1.0}$	26084.6	3.80×10^{-18}	26080.6	3.42×10^{-18}
$\nu_{8.1.0}$	26739.1	3.65×10^{-18}	26740.2	3.53×10^{-18}
$\nu_{9.1.0}$	27394.6	3.42×10^{-18}	27393.9	3.35×10^{-18}
$\nu_{10.1.0}$	28047.7	3.05×10^{-18}	28047.7	2.99×10^{-18}
$\nu_{11.1.0}$	28691.3	2.56×10^{-18}	28689.8	2.49×10^{-18}
$\nu_{12.1.0}$	29336.0	2.00×10^{-18}	29332.0	1.90×10^{-18}
A^2A_2 system: asymmetric stretch				
$\nu_{3.0.2}$	23947.3	1.55×10^{-18}	23934.2	1.33×10^{-18}
$\nu_{4.0.2}$	24630.3	2.85×10^{-18}	24622.7	2.21×10^{-18}
$\nu_{5.0.2}$	25296.7	4.11×10^{-18}	25293.8	3.40×10^{-18}
$\nu_{6.0.2}$	25962.0	5.00×10^{-18}	25959.1	4.61×10^{-18}
$\nu_{7.0.2}$	26615.8	5.64×10^{-18}	26618.7	5.51×10^{-18}
$\nu_{8.0.2}$	27271.0	6.03×10^{-18}	27272.4	5.90×10^{-18}
$\nu_{9.0.2}$	27917.9	5.68×10^{-18}	27920.4	5.58×10^{-18}
$\nu_{10.0.2}$	28559.3	4.95×10^{-18}	28562.6	4.87×10^{-18}
$\nu_{11.0.2}$	29195.3	3.83×10^{-18}	29199.0	3.77×10^{-18}
$\nu_{12.0.2}$	29811.1	2.68×10^{-18}	29806.4	2.61×10^{-18}
A^2A_2 system: asymmetric stretch and bend				
$\nu_{2.1.2}$	23535.1	7.58×10^{-19}	23529.3	5.87×10^{-19}
$\nu_{3.1.2}$	24194.9	9.50×10^{-19}	24200.4	8.49×10^{-19}
$\nu_{4.1.2}$	24892.8	1.31×10^{-18}	24888.8	1.16×10^{-18}
$\nu_{5.1.2}$	25560.7	1.67×10^{-18}	25554.2	1.56×10^{-18}
$\nu_{6.1.2}$	26214.1	1.93×10^{-18}	26213.7	1.86×10^{-18}
$\nu_{7.1.2}$	26871.1	2.00×10^{-18}	26873.2	1.95×10^{-18}
$\nu_{8.1.2}$	27522.6	1.87×10^{-18}	27521.2	1.83×10^{-18}
$\nu_{9.1.2}$	28168.4	1.60×10^{-18}	28169.2	1.55×10^{-18}

The observed positions and values for peak absorption cross-sections for various progressions of the A^2A_2 system of $O^{35}ClO$ for 293 and 213 K at two different resolutions. The positions correspond to the highest cross-section in each vibrational band (not to the bandheads given in Table 2) and they vary with the temperature due to the change of the rotational envelope.

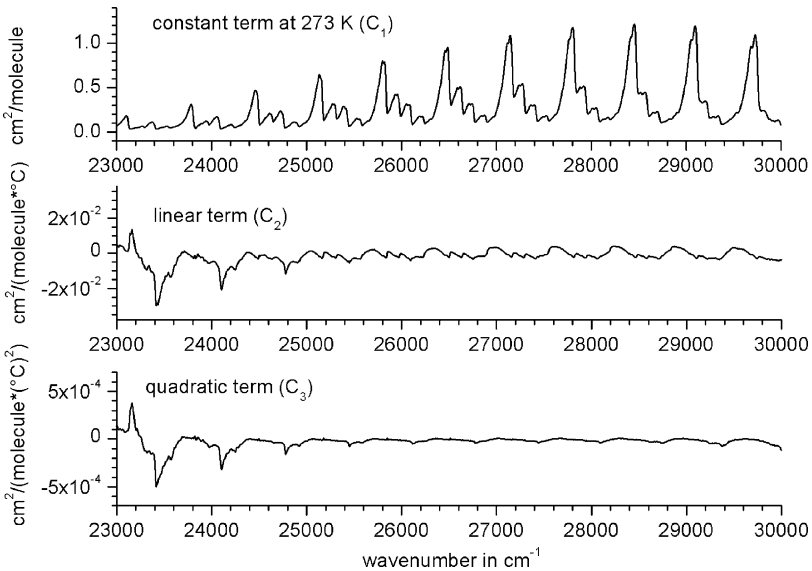

Fig. 8. Coefficients from a least-squares fit according to $\sigma(T) = C_1 + C_2T + C_3T^2$ based on the new OClO cross-sections at all temperatures between 293 and 213 K with a resolution of 20 cm^{-1}.

Table 2
Observed and calculated band centres of $O^{35}ClO$

Upper v_1	State's v_2	Quanta v_3	Observed[a] (cm^{-1})	Calculated (cm^{-1})	Difference (cm^{-1})
3	0	0	23118.0	23121.4	−3.4
2	0	2	23280.0	23278.6	1.4
3	1	0	23393.0	23390.8	2.2
2	1	2	23550.0	23549.4	0.6
4	0	0	23803.0	23806.2	−3.2
3	0	2	23959.0	23958.4	0.6
4	1	0	24072.0	24072.9	−0.9
3	1	2	24227.0	24226.6	0.4
5	0	0	24485.0	24485.7	−0.7
4	0	2	24633.0	24632.9	0.1
5	1	0	24750.0	24749.7	0.3
4	1	2	24896.0	24898.5	−2.5
6	0	0	25162.0	25159.9	2.1
5	0	2	25306.0	25302.2	3.8
6	1	0	25424.0	25421.4	2.6
5	1	2	25564.0	25565.2	−1.2
7	0	0	25832.0	25828.9	3.1
6	0	2	25966.0	25966.3	−0.3
7	1	0	26089.0	26087.7	1.3
6	1	2	26226.0	26226.6	−0.6
8	0	0	26495.0	26492.7	2.3
7	0	2	26623.0	26625.1	−2.1
8	1	0	26748.0	26748.9	−0.9
7	0	2	26881.0	26882.8	−1.8
9	0	0	27151.0	27151.2	−0.2
7	1	2	27277.0	27278.7	−1.7
9	1	0	27404.0	27404.7	−0.7
8	1	2	27532.0	27533.7	−1.1
10	0	0	27803.0	27804.5	−1.5
9	0	2	27928.0	27927.0	1.0
10	1	0	28054.0	28055.4	−1.4
9	1	2	28180.0	28179.4	0.6
11	0	0	28453.0	28452.5	0.5
10	0	2	28568.0	28570.0	−2.0
11	1	0	28698.0	28700.7	−2.7
10	1	2	28824.0	28819.8	4.2
12	0	0	29097.0	29095.2	1.8
11	0	2	29207.0	29207.8	−0.8
12	1	0	29341.0	29340.9	0.1
11	1	2	29457.0	29455.0	2.0
13	0	0	29732.0	29732.8	−0.8

Comparison of the observed and calculated band head positions (in cm^{-1}) for the strongest progressions of $O^{35}ClO$, from $v_1 = 3$ to 13, using the upper state's constants given in Table 3. The average of the differences between observed and calculated band head positions is 0.013 cm^{-1} with a rms deviation for the 41 band centres of 1.85 cm^{-1}.

[a] Observed positions are given with an estimated uncertainty of 3 cm^{-1}.

constants for the OClO upper electronic state (see Tables 2 and 3, where the constants are compared with the experimental values by Hubinger and Nee [20] and with the theoretical values of Peterson [35]). The general agreement between the different studies is good. It should be noted that the anharmonicity constant x_{33} given by Richard and Vaida [19] was used for this fit. The determined constants reproduce the observed spectrum well, and they will be useful for modeling the OClO absorption spectrum at different temperatures using the corresponding band contours (work in progress).

4.2. Photolysis studies

The photolysis experiments were carried out to investigate whether the photolysis of pure OClO leads to a complete conversion into molecular oxygen and chlorine according to the following mechanism:

$$OClO + hv \rightarrow O + ClO \quad (I)$$

$$O + OClO \rightarrow O_2 + ClO \quad (II)$$

$$ClO + ClO \rightarrow Cl_2 + O_2 \quad (II)$$

$$\text{net}: \quad 2OClO + h\nu \rightarrow Cl_2 + 2O_2 \quad (IV)$$

If this mechanism was sufficient to reproduce our measurements (with Cl_2 and O_2 as the only products of OClO photolysis), it would be a second independent method to determine OClO absorption cross-sections at 293 K.

In our experiments the photolysis of OClO resulted in the formation of Cl_2. However only 20–80% (depending on the photolysis conditions) of the initial OClO was converted into Cl_2. Because there were no other initial reactants than OClO (except for an estimated ≤2% residual Cl_2 from the synthesis), these differences can only be explained by the formation of higher chlorine oxides. Indeed molecules like Cl_2O_3 and Cl_2O_4 were previously detected as products of the room temperature photolysis of OClO mixtures [37,38]. Unfortunately, because of the limited spectral range in our observations, there was no possibility of detecting these higher chlorine oxides above 33,000 cm^{-1} (wavelengths below 300 nm).

To investigate which chemical reactions are important in our measurements, chemical model calculations were carried out using the FACSIMILE© software [39]. All reactions available in the literature [37–40] together with rate constants from the NIST [41] or the JPL kinetic databases [42] were integrated into the modelling scheme. The model results were compared to the measurements of the time-dependent concentrations of OClO and Cl_2 in photolysis experiments extending over more than 10 min. The photolysis rates for OClO and Cl_2 were calculated using their absorption cross-sections together with the spectrum of the photolysis lamps.

Different reaction mechanisms were tested to reproduce the observed processes, i.e. the decrease of OClO, the increase of Cl_2 and the chlorine deficit due to the formation of other final products than Cl_2. The first chemical model included only reactions and rate coefficients described in the literature [37,38,41,42]. However this mechanism did not reproduce the data sufficiently well: the OClO decrease was slower than observed and instead of increasing the Cl_2 a further decomposition took place. Consequently, some extensions to the first mechanism were formulated, in particular concerning the formation and decomposition of the higher

Table 3
Spectroscopic constants of the A^2A_2 state of OClO

Upper state's constant	This work (cm^{-1})	Reference [20] (cm^{-1})	Reference [19] (cm^{-1})	Reference [35] (cm^{-1})
T_e	20330.0 ± 3.8	20962[a]	20316.9	20265.7[b]
ω_1	709.61 ± 0.78	735 ± 10	705.9	720.4
ω_2	278.8 ± 2.2	291 ± 6	284.2	288.1
ω_3[c]	421.8 ± 1.2	433 ± 2.5	410.5	419.2
x_{11}	−2.624 ± 0.041	−4.9 ± 0.3	−2.76	−3.61
x_{12}	−2.64 ± 0.22	−3.9 ± 0.7	−3.55	−3.98
x_{13}	−5.10 ± 0.12	−5.0 ± 0.4	−5.47	−50.4
x_{23}	−0.56 ± 0.66	–	−2.22	−6.76
x_{33}	13.15[d]	–	13.15	23.69

Vibrational constants of $O^{35}ClO$ from this work, compared to the experimental work of Richard and Vaida [19], of Hubinger and Nee [20], and to the ab-initio calculation of Peterson [35]. All values are given in cm^{-1}. The values in parentheses indicate 1σ in units of the last digit.

[a] From extrapolation.

[b] Calculated by Peterson [35] using the T_0 of [19].

[c] Derived from $2\omega_3$.

[d] Constant fixed to the value of [19] in the least-squares calculation.

chlorine oxides. However, the observations of OClO and Cl_2 alone do not provide the necessary information to validate these extensions with sufficient accuracy. Therefore, new photolysis experiments are currently carried out in our laboratory to investigate this issue in more detail, focussing on the observation of intermediates like ClO, ClOO and ClO_3 and the potential final products like Cl_2O_3 and Cl_2O_4.

5. Conclusion

In this study the absorption cross-sections of OClO have been measured at five atmospheric temperatures between 213 and 293 K using high-resolution Fourier-transform spectroscopy in the 325–435 nm (23,000–31,000 cm^{-1}) region. The obtained data is characterised by an accurate wavelength calibration and high spectral resolution (1.0 cm^{-1}).

The spectra have been vibrationally assigned and molecular constants of the upper electronic state were re-determined, in good agreement with those of Hubinger and Nee [19] and Richard and Vaida [20].

The new OClO cross-sections are important for atmospheric remote-sensing using optical spectroscopy in order to reduce systematic errors in the data retrieval, which are mainly due to wavelength calibration uncertainties of the reference spectra and to unmatched instrumental line-shapes between the atmospheric and the laboratory reference spectra. The new FTS cross-sections have already been successfully employed in the analysis of ground- and balloon-based atmospheric measurements, and they have led to an improved data quality for these and other applications. They will also be used for modelling the OClO $\tilde{A} - \tilde{X}$ electronic bands from molecular constants (work in progress).

All new OClO cross-sections and polynomial coefficients for temperature interpolation can be obtained as ASCII files via HTML from the internet (http://www.iup.physik.uni-bremen.de) or upon request to one of the authors.

Acknowledgements

This study was supported by the German Space Agency (formerly DARA, now GSF) by grant No. 95-EP-9201 ("SCIAMACHY Scientific Study") and by the University and Bundesland of Bremen. J. O. whishes to thank the "Deutsche Forschungsgemeinschaft" (DFG) for a research fellowship in frame of the new "Emmy-Noether" program. The excellent technical assistance of Bruker GmbH Germany merits particular mention.

References

[1] R.P. Wayne, Chemistry of the Atmospheres, second ed., Clarendon Press, Oxford, 1991.
[2] NOAA, NASA, UNEP, WMO and CEC (Eds.), World Meteorological Organization, Global Ozone Research and Monitoring Project—Report No. 44, Geneva, 1999.
[3] S. Salomon, Rev. Geophys. 37 (1999) 275–315.
[4] S. Solomon, Nature 321 (1986) 755–760.
[5] S. Solomon, R.W. Sanders, H.L. Miller, J. Geophys. Res. D 95 (1990) 13807–13812.
[6] S.P. Sander, R.R. Friedl, Geophys. Res. Lett. 15 (1988) 887–891.
[7] R. Toumi, Geophys. Res. Lett. 21 (1994) 1487–1490.
[8] A. Wahner, C. Schiller, J. Geophys. Res. D 97 (1992) 8047–8055.
[9] R.W. Sanders, S. Solomon, J.P. Smith, L. Perliski, H.L. Miller, G.H. Mount, J.G. Keys, A.L. Schmeltekopf, J. Geophys. Res. D 98 (1993) 7219–7228.
[10] J.-B. Renard, F. Lefevre, M. Pirre, C. Robert, D. Huguenin, J. Atmos. Chem. 26 (1997) 65–76.
[11] M. Eisinger, J.P. Burrows, A. Richter, in: Proceedings of the GOME Geophysical Validation Campaign-Final Results Workshop, Noordwijk, The Netherlands, ESA WPP-108, 1996, pp. 93–105.
[12] F. Wittrock, A. Richter, J.P. Burrows, in: Proceedings of the 1st European Symposium on Atmospheric Measurements from Space (ESAMS), ESA-ESTEC, Noordwijk, The Netherlands, ESA WPP-161, vol. 2, 1999, pp. 735–738.
[13] F. Erle, A. Grendel, D. Perner, U. Platt, K. Pfeilsticker, Geophys. Res. Lett. 25 (1998) 4329–4332.
[14] U. Platt, D. Perner, H.W. Patz, J. Geophys. Res. C 84 (1979) 3329–3336.

[15] S. Solomon, A.L. Schmeltekopf, R.W. Sanders, J. Geophys. Res. D 92 (1987) 8311–8319.
[16] J. Orphal, K. Bogumil, A. Dehn, B. Deters, S. Dreher, O.C. Fleischmann, M. Hartmann, S. Himmelmann, T. Homann, H. Kromminga, P. Spietz, A. Türk, A. Vogel, S. Voigt, J.P. Burrows, laboratory spectroscopy in support of UV-Visible remote-sensing of the atmosphere, in: Recent Research Developments in Physical Chemistry, vol. 6, Transworld Research Network, Trivandrum, 2002, pp. 15–34.
[17] A. Wahner, G.S. Tyndall, A.R. Ravishankara, J. Phys. Chem. 91 (1987) 2734–2738.
[18] G.J. Frost, L.M. Goss, V. Vaida, J. Geophys. Res. D 101 (1996) 3879–3884.
[19] E. C Richard, V. Vaida, J. Chem. Phys. 94 (1991) 153–162.
[20] S. Hubinger, J.B. Nee, Chem. Phys. 181 (1994) 247–257.
[21] G. Marston, I.C. Walker, N.J. Gingell, H. Zhao, K.L. Brown, F. Motte-Tollet, J. Delwiche, M.R.F. Siggel, J. Phys. B: At. Mol. Opt. Phys. 31 (1998) 3387–3405.
[22] S. Voigt, S. Dreher, J. Orphal, J.P. Burrows, J. Mol. Spectrosc. 180 (1996) 359.
[23] S. Gerstenkorn, P. Luc, Atlas du Spectre d'Absorption de la Molécule d'Iode, Editions du CNRS, Paris, 1978.
[24] A. Türk, Diploma Thesis, University of Bremen, 1994.
[25] J.P. Burrows, A. Dehn, J. Orphal, A. Türk, B. Deters, A. Richter, S. Voigt, M. Weissenmayer, S. Himmelmann, D. Perner, Final Report for the European Space Agency ESA (ESTEC), University of Bremen, 1997.
[26] A. Dehn, Diploma Thesis, University of Bremen, 1995.
[27] K. Bogumil, J. Orphal, S. Voigt, H. Bovensmann, O.C. Fleischmann, M. Hartmann, T. Homann, P. Spietz, J.P. Burrows, in: Proceedings of the 1st European Symposium on Atmospheric Measurements from Space (ESAMS), ESA-ESTEC, Noordwijk, The Netherlands, ESA WPP-161, vol. 2, 1999, pp. 443–447.
[28] R.I. Derby, W.S. Hutchinson, Inorg. Synth. 4 (1953) 152.
[29] J. Orphal, S. Voigt, J.P. Burrows, in: Proceedings of XIV International Conference on High-Resolution Molecular Spectroscopy, Prague, Czech Republic, 1996.
[30] J. Brion, A. Chakir, D. Daumont, J. Malicet, C. Parisse, Chem. Phys. Lett. 213 (1993) 610–612.
[31] J.P. Burrows, A. Dehn, B. Deters, S. Himmelmann, A. Richter, S. Voigt, J. Orphal, J. Quant. Spectrosc. Rad. Transf. 60 (1998) 1025–1031.
[32] J.P. Burrows, A. Dehn, B. Deters, S. Himmelmann, A. Richter, S. Voigt, J. Orphal, J. Quant. Spectrosc. Rad. Transf. 61 (1999) 509–517.
[33] M.A.A. Clyne, J.A. Coxon, Proc. R. Soc. London, A 303 (1968) 207–231.
[34] N. Basco, S.K. Dogra, Proc. R. Soc. London, A 323 (1971) 2968–2982.
[35] K.A. Peterson, J. Chem. Phys. 109 (1998) 8864–8875.
[36] J. Orphal, in preparation.
[37] F. Zabel, Ber. Bunsenges. Phys. Chem. 95 (1991) 893–900.
[38] J.B. Burkholder, R.L. Mauldin III, R.J. Yokelson, S. Solomon, A.R. Ravishankara, J. Phys. Chem. 97 (1993) 7597–7605.
[39] FACSIMILE, Process and Chemical Reaction Modeller, vol. 3.0, AEA Technology, Harwell, UK, 1994.
[40] R.P. Wayne, G. Poulet, P. Briggs, J.P. Burrows, R.A. Cox, P.J. Crutzen, G.D. Hayman, M.E. Jenkin, G. Le Bras, G.K. Moortgat, U. Platt, R.N. Schindler, Atmos. Environ. 29 (1995) 2675–2884.
[41] NIST Standard Reference Database 17-2Q98, Data through 2nd quarter, 1998.
[42] W.B. DeMore, S.P. Sander, D.M. Golden, R.F. Hampson, M.J. Kurylo, C.J. Howard, R.A. Ravishankara, C.E. Kolb, M.J. Molina, Chemical Kinetics and Photochemical Data for Use in Stratospheric Modeling, No. 12, JPL Publication 97-4, 1997.